

# Overdetermined Least-Squares Aberration Estimates Using Common-Midpoint Signals

Mark A. Haun\*, *Member, IEEE*, Douglas L. Jones, *Fellow, IEEE*, and William D. O'Brien, Jr., *Fellow, IEEE*

**Abstract**—As medical ultrasound imaging moves to larger apertures and higher frequencies, tissue sound-speed variations continue to limit resolution. In geophysical imaging, a standard approach for estimating near-surface aberrating delays is to analyze the time shifts between common-midpoint signals. This requires complete data—echoes from every source/receiver pair in the array. Unfocused common-midpoint signals remain highly correlated in the presence of delay aberrations; there is also tremendous redundancy in the data.

In medical ultrasound, this technique has been impaired by the wide-angle, random-scattering nature of tissue. This has made it difficult to estimate azimuth-dependent aberration profiles or to harness the full redundancy in the complete data. Prefiltering the data with two-dimensional fan filters mitigates these problems, permitting highly overdetermined, least-squares solutions for the aberration profiles at many steering angles. In experiments with a tissue-mimicking phantom target and silicone rubber aberrators at nonzero stand-off distances from a one-dimensional phased array, this overdetermined, fan-filtering algorithm significantly outperformed other phase-screen algorithms based on nearest-neighbor cross-correlation, speckle brightness maximization, and common-midpoint signal analysis.

Our results imply that there is still progress to be made in imaging with single-valued focusing operators. It also appears that the signal-to-noise penalty for using complete data sets is partially compensated by the overdetermined nature of the problem.

**Index Terms**—Common-midpoint signals, medical ultrasound imaging, phase-aberration correction, signal redundancy.

## I. INTRODUCTION

MUCH ATTENTION has been given to improving the spatial resolution of medical ultrasound by using higher frequencies and/or increasing the size of the transducer aperture. The attenuation properties of tissue impose an upper limit on frequency, yet under this constraint, diffraction theory still permits a significant improvement in resolution over current systems.

The principal obstacle to improved resolution is the spatial variation of sound speed in tissue. The speed of sound ranges from about 1470 m/s in fatty tissues to over 1600 m/s in muscle and connective tissue and up to 3700 m/s in bone [1], [2]. Although medical ultrasound imaging depends on the echoes generated by scattering from impedance discontinuities, including

changes in the speed of sound, current systems assume a bulk homogeneity—that is, weak scattering, straight raypaths, and a constant speed of sound at scales above a wavelength. When these assumptions fail, imaging resolution suffers as the point spread function widens. High sidelobes are especially harmful, compromising the imaging system's ability to resolve small, negative-contrast regions surrounded by speckle. These effects have been well documented, e.g., when imaging through the abdominal wall [3], [4], and the female breast [5], [6].

From the beamformer's point of view, large-scale sound-speed variations, multipathing, multiple scattering and reverberation, constructive and destructive interference along diffracting wavefronts, and frequency-dependent attenuation all act to shift and distort the waveforms that would have been expected in an idealized model. If nonlinear propagation is neglected, the aberrating effects of tissue can be thought of as a time- and space-variant linear filtering operation at the aperture. The full restoration of diffraction-limited imaging will require such a general model. Efforts toward full aberration correction include time-reversal focusing [7], [8], optimal inverse filtering [9], [10], models consisting of multiple, thin, aberrating screens [11], and blind multichannel deconvolution [12]. The latter two are noteworthy because they do not require point targets for clinical, pulse-echo imaging. (Point targets are frequently not available in medical ultrasound images.)

Due to the difficulty of estimating a large number of model parameters, most of the algorithms proposed for aberration correction *in vivo*, including the one described in this paper, have approximated the hypothetical per-channel filters as pure time delays, ignoring the effects of waveform distortion and usually amplitude fluctuations as well [13]–[23]. This is known as the near-field phase-screen model, because the aberration is modeled entirely by variable time delays on the received and transmitted signals due to an infinitesimally thin screen at the face of the transducer array. The term “phase aberration” is frequently used in this context even though the transmit pulses are wide-band; the linear relationship between phase and frequency is implied.

The time delays along the aperture are called the aberration profile. If the aberration profile can be estimated correctly, focusing is easily accomplished by adding compensating delays to the hyperbolic curves dictated by geometry alone. For two-dimensional (2-D) imaging with a one-dimensional (1-D) array

$$\tilde{t}_k(x', z') = t_k(x', z') + \tau_k \quad (1)$$

$$= \frac{1}{c} \sqrt{(x_k - x')^2 + z'^2} + \tau_k. \quad (2)$$

Here,  $x_k$  is the position of the  $k$ th array element, and  $(x', z')$  is the target location. For a constant sound speed  $c$ , the one-way travel times  $\{t_k\}$  define a hyperbola in the  $(x, t)$  space of the

Manuscript received March 19, 2004; revised May 17, 2004. The Associate Editor responsible for coordinating the review of this paper and recommending its publication was A. Manduca. Asterisk indicates corresponding author.

\*M. A. Haun is with Philips Research, Briarcliff Manor, NY 10510 USA (e-mail: haunma@keteu.org).

D. L. Jones and W. D. O'Brien are with the Department of Electrical and Computer Engineering, University of Illinois at Urbana-Champaign.

This work was supported by the University of Illinois Research Board and the National Institutes of Health (Grant no. CA79179).

Digital Object Identifier 10.1109/TMI.2004.831792

recorded data. These may be viewed as a focusing operator for the point  $(x', z')$ , where the array elements are fired at times  $\{-t_k\}$  for transmit focusing, the reflection occurs at time zero, and the received echoes are coherently summed at times  $\{t_k\}$  for receive focusing [24]. The aberration profile,  $\{\tau_k\}$ , is added to  $\{t_k\}$  to form  $\{\tilde{t}_k\}$ , the correct focusing operator in the presence of delay aberrations. Casting this into the more general framework of per-channel filtering,  $\{\tilde{t}_k\}$  may be described as a single-valued focusing operator, because the  $k$ th filter's impulse response is merely a shifted spike, the shift being given by  $\tilde{t}_k$ .

Many phase-aberration correction algorithms estimate  $\tilde{t}$  directly; in this case, we define the aberration profile  $\tau$  as the difference between  $\tilde{t}$  and its best-fit hyperbola (in the least-squares sense). The parameters of the best-fit hyperbola can also provide an estimate of the focus location  $(x', z')$ , which may have drifted from some initial location as the algorithm was iterated.

The phase-screen model has been used successfully in a number of imaging disciplines. In seismic imaging, for example, aberrating delays known as "statics" are caused by a variable-thickness "weathered layer" of slow sound-propagation speed between the Earth's surface and deeper, higher-speed rock layers [25]. This layer may be reasonably treated as a thin screen [26], [27]. In medical ultrasound, however, the near-field phase-screen model is not such a good approximation to physical reality. Although the principal aberrators may be located close to the transducer in some cases, they are not thin with respect to the distance between transducer and target, and waveform distortion effects will occur in addition to the delays predicted by the model. A modified phase-screen model can partially compensate for these effects by backpropagating the received signals some distance from the transducer face before estimating the aberration profile [28]. This approach could be applied to any of the phase-aberration correction algorithms discussed here, but it was not used in our experiments.

If waveform distortions and multipathing effects could be neglected, good correction could still be achieved by calculating as many different aberration profiles as necessary for various parts of the image. Each region where the modeled aberration is reasonably constant is termed an isoplanatic patch; within the general framework of single-valued focusing operators, these patches may be arbitrarily small. It is interesting to note that an optimal choice of single-valued focusing operators has been shown to yield high-quality seismic images, where the aberrations are much more severe than in soft tissue [29]. It is possible that further gains in ultrasound image quality (beyond that which has been demonstrated) are attainable under a single-valued focusing operator assumption.

#### A. Focused Transmits vs. Common-Midpoint Signals

The best-studied class of correction algorithms based on the phase-screen model is exemplified by the nearest-neighbor cross-correlation (NNCC) approach of Flax and O'Donnell [13], [14]. A focused transmit pulse is aimed at some region of interest, and the received signals on neighboring array elements are cross-correlated to estimate the relative time shifts. These time shifts are integrated across the aperture and taken as an improved focusing operator. Because the original transmit focus is degraded by uncompensated aberration, the procedure

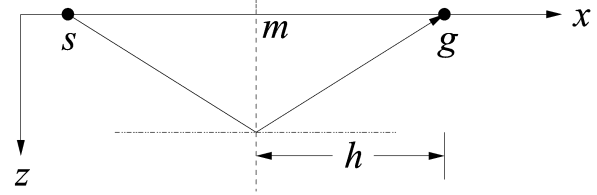


Fig. 1. A simple reflection experiment defining the positions of transmit element  $s$ , receive element  $g$ , midpoint  $m$ , and offset  $h$ .

is iterated with the expectation of convergence to the correct focusing operator.

Algorithms of this type have the advantage of estimating aberration profiles from small regions of tissue; thus, small isoplanatic patch size should not be a problem. If a single scatterer dominates the focal region, the received signals are highly correlated and the algorithm performs well. Unfortunately, dominant point scatterers are scarce in medical ultrasound images. Speckle-generating tissues, which contain many random scatterers within the focal region of an ultrasound transducer, are far more common. In this case, the spatial correlation of the received signals can be predicted with a form of the van Cittert-Zernike theorem [30], [31], which treats the random scattering region at the focus as a source of incoherent radiation. If the transmitted pulse is well-focused, adjacent element signals are highly correlated. Phase aberration drastically reduces the correlation between adjacent signals and, if severe enough, can prevent convergence. This weakness has been addressed by the translating apertures (TA) algorithm [15], which can be viewed as a hybrid approach between the full-aperture focus in NNCC and the common-midpoint concept discussed next.

A different approach to phase-aberration correction exploits the redundant information contained in "complete" data [19], [20]. A complete data set  $d_{s,g}(t)$  has  $N^2$  signals, one for each possible combination of one transmit element  $s$  and one receive element  $g$  in an  $N$ -element array. These data may be used to implement any image formation algorithm offline using synthetic aperture techniques. The data are also highly redundant; one could, for example, form  $N$  independent images of the target, one per transmit element. It is convenient to order this redundancy through the coordinate transformation (Fig. 1)

$$m = \frac{g + s}{2} \quad (\text{midpoint}) \quad (3)$$

$$h = \frac{g - s}{2} \quad (\text{offset}). \quad (4)$$

The set of signals  $d_{m-h, m+h}(t)$ , with  $m$  constant, is called a common-midpoint gather [32]. The signals on a common-midpoint gather are highly correlated, making them attractive for estimating aberration profiles (Fig. 2). The starting point for these calculations is a collection of estimated time shifts between signals within the common-midpoint gathers. Usually, to estimate the time shift between two signals, the displacement from zero of the peak in the signals' cross-correlation function is used.

Algorithms based on common-midpoint signal analysis are less susceptible to misconvergence than those requiring an initial transmit focus, because common-midpoint signals remain highly correlated even in the presence of phase aberration. The process of transmit focusing (summing  $d_{s,g}(t)$  over  $s$ ) assumes knowledge of the correct focusing operator; if this assumption is incorrect, useful information is irretrievably lost. By analyzing

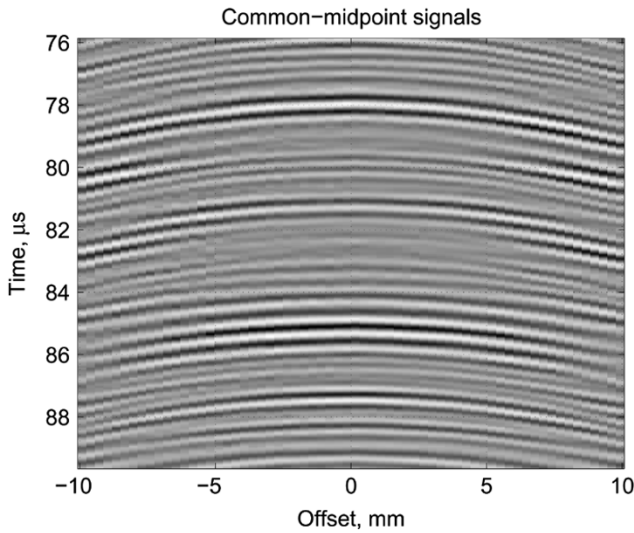


Fig. 2. A common-midpoint gather obtained from speckle-producing phantom data. The strong correlation between signals at different offsets is evident.

the common-midpoint gathers prior to focusing, the extra information can be used to derive a more robust solution.

An automated method for estimating phase-screen parameters from complete data was first developed in the context of the “statics” problem in seismic imaging [26]. This work modeled the aberrating delays (the statics) as a rapidly varying, zero-mean random sequence. By placing the time-shift estimates into a matrix with  $s$  and  $g$  axes, crude estimates of the aberrating delays were obtained by averaging individual rows or columns. Later, the problem was re-examined and cast into a least-squares framework [27].

Rachlin [19] was the first to recognize the potential of common-midpoint signals in medical ultrasound imaging. He explained the redundancy of common-midpoint signals using a far-field approximation in which these signals sample the same portion of the target’s Fourier transform. His algorithm estimates the pair-wise time shifts between many signals in each common-midpoint gather. These time-shift estimates define a system of linear equations in the unknown aberrating delays. In a complete data set collected using an  $N$ -element array, if all pair-wise time-shift estimates are used, a total of

$$N_e = \frac{N^3}{12} - \frac{N^2}{8} - \frac{N}{12} \quad (5)$$

equations may be written in the  $N$  unknowns [33]. Clearly, the system is highly overdetermined even if all but the highest-quality shift estimates are discarded.

Time shifts on a common-midpoint gather derive not only from phase aberration, but also from the source-receiver offset and the location of the reflecting target(s). If the aberrating delays are to be estimated accurately, the latter two effects must be properly accounted for. If reflections occur directly below the midpoint, as they would for a flat reflector at depth  $z'$  (Fig. 1), the travel time  $t$  versus offset  $h$  is

$$t = \frac{2}{c} \sqrt{\left(\frac{g-s}{2}\right)^2 + z'^2} \quad (6)$$

$$= \frac{2}{c} \sqrt{h^2 + z'^2} \quad (7)$$

which is a hyperbola in  $(h, t)$  space, that is, on a common-midpoint gather. In the seismic imaging community, the delay with increasing offset is called *normal moveout* (NMO) [32]. A time-stretching and shifting operation called NMO correction

$$t \rightarrow t', \quad \text{where } t' = \sqrt{t^2 + \frac{4h^2}{c^2}} \quad (8)$$

should be applied to remove this geometric delay and flatten the hyperbolas before attempting to cross-correlate the signals. Rachlin’s early work in medical ultrasound [19] was based on a far-field assumption which neglected NMO.

Although it is usually possible to find flat reflectors in seismic data, these are rare in biological tissue. In medical ultrasound imaging, the bulk of the reflection energy comes from countless sub-wavelength scatterers, and reflection energy typically returns to the transducer from many directions simultaneously. Thus, in the development of the near-field signal redundancy (NFSR) algorithm [20], Li recognized the need to extend NMO correction to angles away from the array normal ( $\theta \neq 0^\circ$ ). His generalized moveout correction for scatterers at angle  $\theta$ , called the “dynamic near-field delay correction,” defines the change of variable  $t \rightarrow t'$ , where

$$t' = \sqrt{\left(\frac{t}{2}\right)^2 + \frac{h^2}{c^2} - t\frac{h}{c} \sin \theta} + \sqrt{\left(\frac{t}{2}\right)^2 + \frac{h^2}{c^2} + t\frac{h}{c} \sin \theta}. \quad (9)$$

Unfortunately, this operation by itself does nothing to suppress echoes coming from azimuths other than  $\theta$ . In the no-aberration case, all reflections on the corrected common-midpoint gathers should be perfectly flat, but these off-axis echoes will not be straightened out; this will cause an undesirable bias in the time-shift estimates. The moveout correction grows rapidly with increasing offset  $h$ , and so does the bias from uncorrected, off-axis scatterers. The problem is particularly severe for arrays with small elements having wide radiation patterns in azimuth.

Due to the wide-angle nature of ultrasound imaging, it frequently happens that one aberration profile only applies to a part of the image. This is the concept of an isoplanatic patch, discussed in the previous section. Multiple, independent profiles must be derived for different azimuth angles (and, less frequently, for different ranges). Thus, the lack of directionality in the processing discussed so far is a compound problem: First, how can the echoes from different azimuths be separated in order to derive independent aberration profiles? Second, even if the aberration profile is not  $\theta$ -dependent, how can bias be eliminated in the time-shift estimates, given that the generalized moveout correction (9) only corrects the common-midpoint gathers for one azimuth at a time, but echoes from many azimuths are present?

Li’s NFSR algorithm [20], [21] addressed this problem by only considering the time shifts between signals of offset 0 and 1 element (after applying the moveout correction). This largely succeeds in avoiding time-shift estimation bias, and the resulting set of  $N - 2$  equations is sufficient to find the aberration profile to within an unknown linear tilt; however, the algorithm has to ignore the wealth of redundant information contained in the longer offsets. Furthermore, it has difficulty finding different aberration profiles at different azimuth angles when used with a small-element array. A modified version of NFSR [22], [23] uses focused subarrays to achieve some directionality. This is effective but has the drawback of reducing

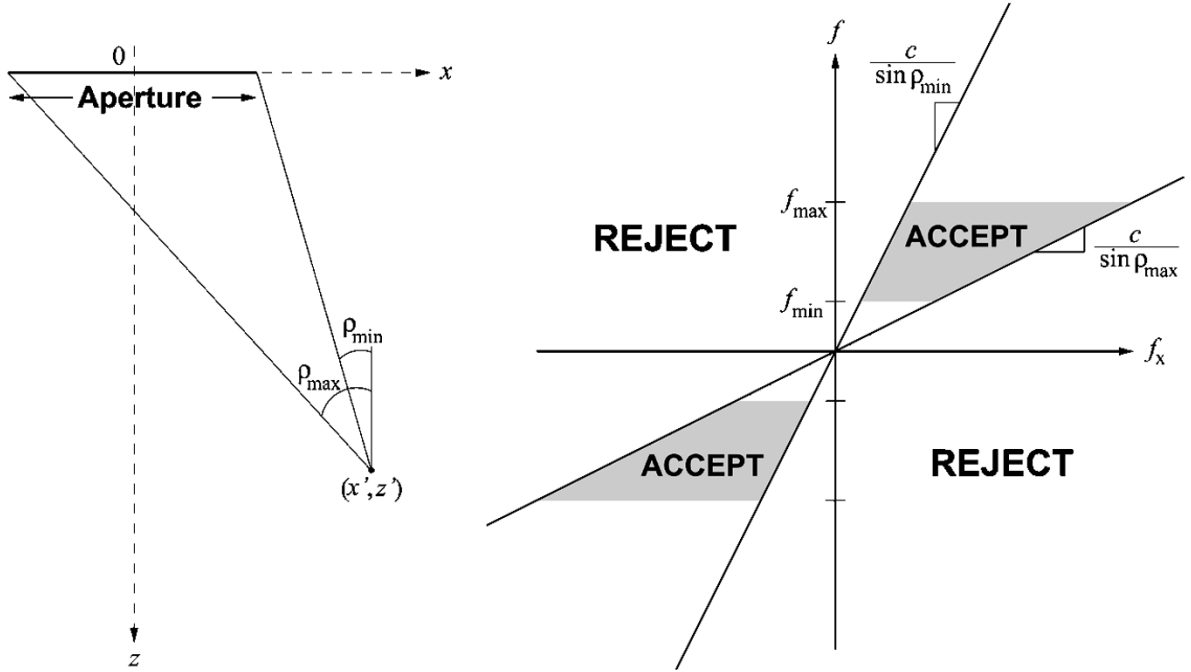


Fig. 3. The signals received along a linear array from a point source or point reflector occupy a fan-shaped region in the 2-D Fourier domain.

the resolution of the estimated aberration profile, because the elements of each subarray are assumed to share the same time shift. It also still precludes the use of a large offset spread to achieve a robust, overdetermined system.

In what follows, the directionality problem is addressed in a new way using 2-D fan filters. After introducing fan filters as an aid to angle selection, the next section analyzes the effect that phase aberration has on their performance. Next, the implementation of the overdetermined, fan-filtering (OFF) algorithm is described. OFF is then compared experimentally with the NFSR subarray algorithm and two other published phase-screen algorithms. This leads to some observations and conclusions.

## II. ANGLE PRESELECTION USING 2-D FAN FILTERS

Consider a point source located at  $(x', z')$ , representing the reflection from a point target at time zero (Fig. 3). Using continuous functions for simplicity, let  $p(t)$  be the transmitted pulse and  $\tau(x)$  the time-shift aberration profile across the aperture. In a medium with a constant speed of sound beyond the near-field phase screen, and neglecting amplitude factors, the aberrated signal received across the array is

$$\tilde{d}(x, t) = p \left[ t - \frac{1}{c} ((x - x')^2 + z'^2)^{1/2} - \tau(x) \right]. \quad (10)$$

Fourier transforming in time, we have

$$\tilde{D}(x, F) = P(F) \exp \left[ \frac{-j2\pi F}{c} ((x - x')^2 + z'^2)^{1/2} - j2\pi F \tau(x) \right] \quad (11)$$

Because only the phase of  $\tilde{D}$  depends on  $x$ , the instantaneous spatial frequency  $F_x$  may be found from the derivative of this phase with respect to  $x$ . For the case of no aberration

$$F_x = \frac{1}{2\pi} \frac{\partial \phi_D}{\partial x} \quad (12)$$

$$= -\frac{F}{c} \frac{x - x'}{((x - x')^2 + z'^2)^{1/2}} \quad (13)$$

$$= \frac{F}{c} \sin \rho \quad (14)$$

where  $\rho$  is defined in Fig. 3. Thus, the unaberrated spectrum from a point target is contained within the fan-shaped regions determined by the temporal bandwidth and the spatial extent of the aperture. (The effect of phase aberration is considered in Section II-B.) If  $\delta_t$  and  $\delta_x$  are the sampling period and array pitch, respectively, then using  $f$  and  $f_x$  as the frequency variables in the discrete-time and discrete-space Fourier domain

$$f_x = f \frac{\delta_x \sin \rho}{\delta_t c}. \quad (15)$$

### A. Implementation

In geophysical imaging, where the subsurface is commonly modeled as a series of linear interfaces between rock layers, digital fan filters defined by (15) are called *dip filters* [32]. This is because echoes from a specular reflecting interface come from an angle equal to the dipping angle of that interface. Ultrasound targets, by contrast, are better viewed as random distributions of point scatterers. Thus, fan filters can be used to discard the echoes from all but one image region, such as that being targeted for aberration correction.

While there are various techniques available for designing 2-D finite impulse response (FIR) fan filters, a design method based on circularly symmetric windows [34] was found to give good results for a wide range of filter angles (Fig. 4).

Fig. 5 illustrates the application of fan filters to data obtained experimentally from a tissue-mimicking phantom (with no aberration) and moveout-corrected for two different correction angles:  $0^\circ$  and  $40^\circ$  from the array normal. The bottom panels are obtained as follows: First, fan filters are applied to the raw data by separately filtering each set of received signals across the

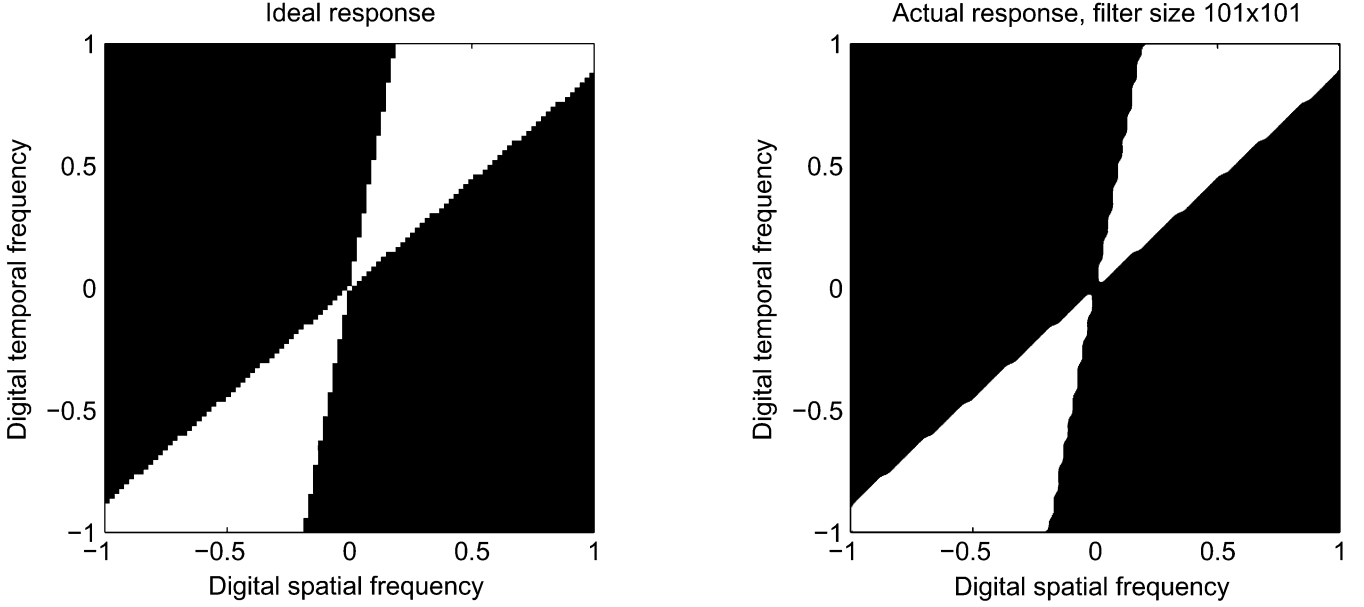


Fig. 4. Ideal and actual fan-filter responses in the digital frequency domain for removing all plane wave components except those from  $\theta = 2^\circ$  to  $12^\circ$ . The FIR filter was obtained with a window design method. White is one and black is zero on this linear scale.

array when transmitting from one element.  $N$  different fan filters are used on these  $N$  wavefields, each one designed to pass a fixed angular range centered on the angle determined by the transmitting element and the center of the scattering region. Then, a set of common-midpoint signals are selected from the filtered complete data set. Finally, the generalized moveout correction is applied.

Notice that in the unfiltered, upper panels, the same echoes are dominant; the effect of the moveout correction is merely to flatten some echoes and under- or over-correct others. After passing the complete data set through fan filters targeting scatterers at  $0^\circ$  and  $40^\circ$  with an angular bandwidth of  $10^\circ$ , the common-midpoint signals appear at first to be of lower quality; notice, however, that *different echoes are dominant* at each angle. If angle-dependent phase aberration were present, different time shifts would be observed in each lower panel.

### B. Effect of Aberration

The claims made for the benefits of fan filtering have, thus far, neglected the effects of phase aberration. Now suppose that  $\tau(x)$  is not zero. Letting  $\tilde{D}$  and  $D$  denote the received signals' 2-D spectra in the aberrated and unaberrated cases, respectively, application of the frequency-convolution property yields

$$\tilde{D}(F_x, F) = D(F_x, F) * U(F_x, F) \quad (16)$$

where

$$U(F_x, F) = \mathcal{F}_x \left[ e^{-j2\pi F \tau(x)} \right] \quad (17)$$

$\mathcal{F}_x[\cdot]$  denotes the spatial Fourier transform, and the convolution is in  $F_x$ . The effect of phase aberration, then, is to convolve the original spectrum in lateral spatial frequency with that of a phase-modulated signal. The spectrum of phase-modulated sig-

nals cannot, in general, be found analytically; some approximate results are known, however [35].

Suppose the aberration profile,  $\tau(x)$ , can be modeled as a Gaussian random process obtained by passing white Gaussian noise through the low-pass filter defined by

$$h(x) = e^{-\pi a^2 x^2}. \quad (18)$$

The autocorrelation function of  $\tau(x)$  is then

$$r_\tau(x) = \frac{1}{a\sqrt{2}} e^{-\pi a^2 x^2 / 2} \quad (19)$$

with the power spectral density

$$T(F_x) = \frac{1}{a^2} e^{-2\pi F_x^2 / a^2}. \quad (20)$$

Defining the aberrator correlation length  $x_0$  as the width of  $r_\tau(x)$  at half maximum, we have

$$a = \frac{1}{x_0} \sqrt{\frac{8 \ln 2}{\pi}}. \quad (21)$$

Following the derivation in [35] for phase modulation by a Gaussian random process, define the mean-square bandwidth of the aberration process  $\tau(x)$

$$W_T = \sqrt{\frac{\int_{-\infty}^{\infty} F_x^2 T(F_x) dF_x}{\int_{-\infty}^{\infty} T(F_x) dF_x}}. \quad (22)$$

The mean-square bandwidth of the phase-modulated signal  $U$  in spatial frequency is then

$$W_U = \frac{F}{x_0} \sqrt{\frac{8 \ln 2}{L} \int_{-L/2}^{L/2} \tau^2(x) dx} \quad (23)$$

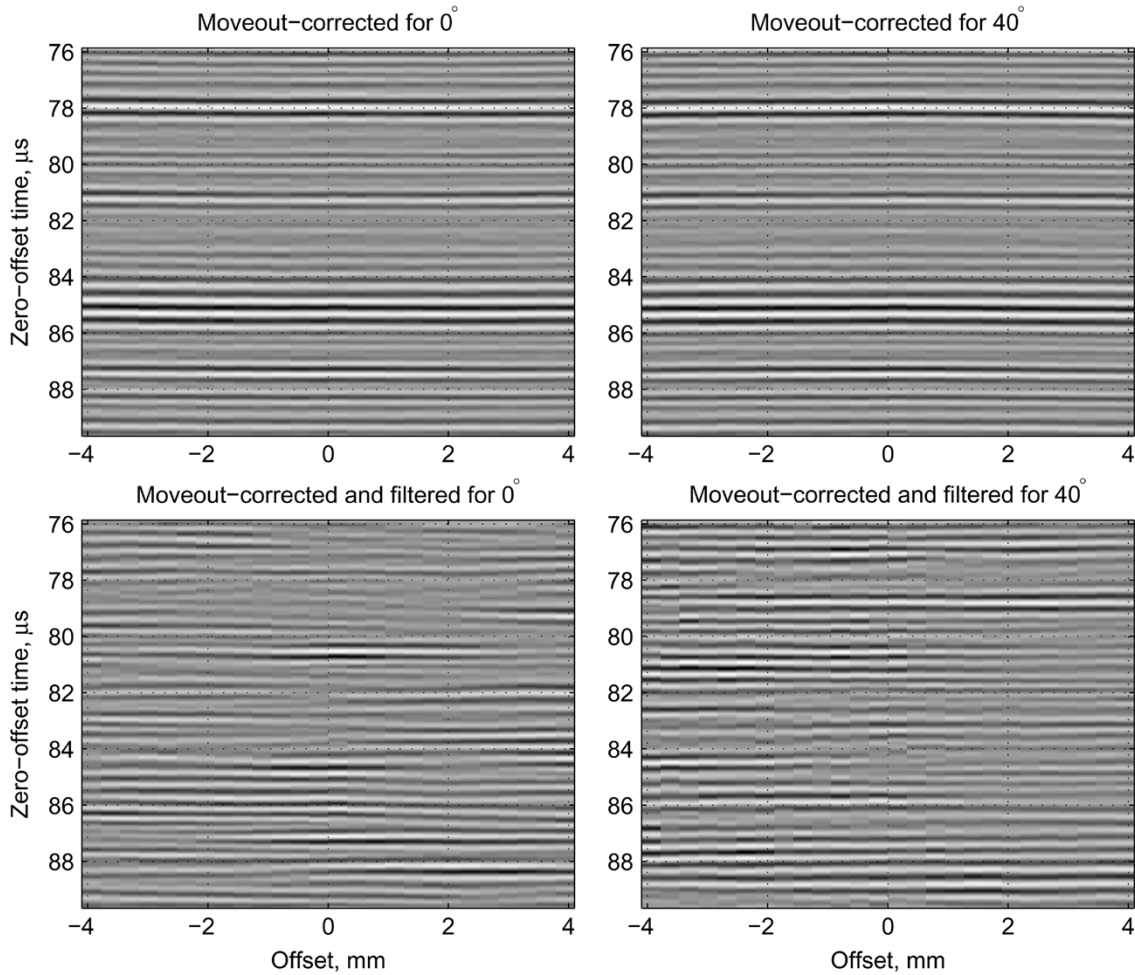


Fig. 5. Common-midpoint signals corrected for scatterers at  $0^\circ$  and  $40^\circ$  from the array normal, and constructed from filtered or unfiltered wavefields. Only when using the appropriate 2-D FIR fan filters are different echoes observed at each angle.

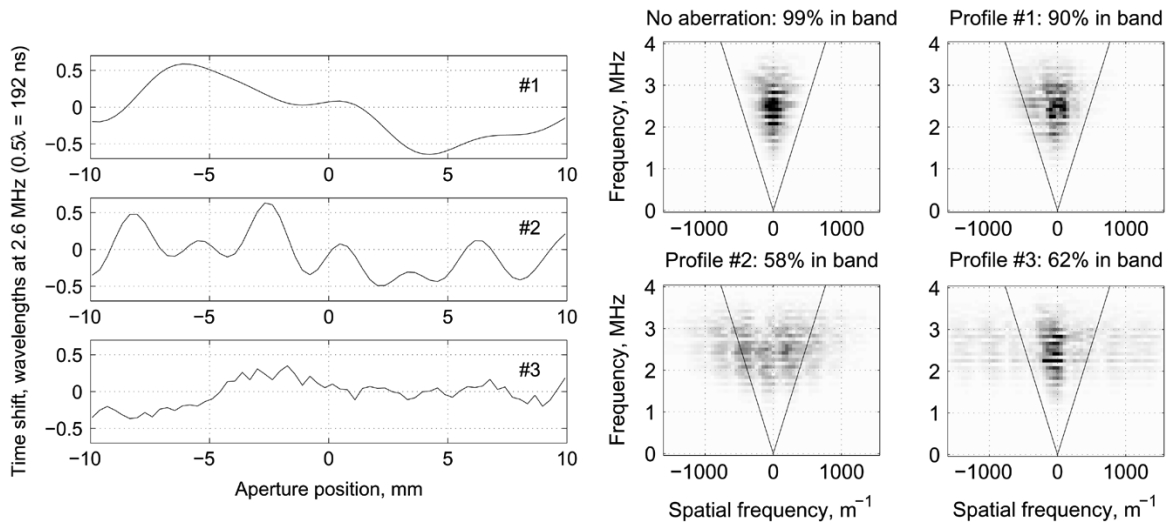


Fig. 6. The effect of phase aberration in the 2-D Fourier domain is to convolve a target's unaberrated spectrum in lateral spatial frequency with a spreading function, the spectrum of a sinusoid phase-modulated by the aberration profile. The spreading becomes worse as the aberration profile fluctuates more rapidly and as its amplitude increases.

where  $L$  is the aperture length. The spatial-frequency spreading effect of phase aberration is, thus, inversely proportional to the aberrator correlation length and proportional to its rms strength.

There is qualitative agreement between this result and the examples considered in Fig. 6. Simulated speckle data were collected from a  $10^\circ$ -wide swath of scatterers, broadside to and 55 mm from a 64-element array. When no aberration is

TABLE I  
OVERDETERMINED LEAST-SQUARES SOLUTION FOR THE ABERRATION PROFILE AT  $(x_{\text{ROI}}, z_{\text{ROI}})$

---

Define $d_{s,g}(t)$	= signal at element $g$ after firing element $s$
$d_g(t; s)$	= set of $N$ signals received on all elements after firing element $s$
$x_s$	= lateral position of array element $s$
$h_{\min}, h_{\max}$	= minimum and maximum offsets to consider in each common-midpoint gather

For  $s = 1 \dots N$  {

Filter  $d_g(t; s)$  with fan filter passing angles  $\rho \pm \Delta\rho$ , where  $\rho = \arctan\left(\frac{x_{\text{ROI}} - x_s}{z_{\text{ROI}}}\right)$ .

}

For  $m = 1 \dots N$  {

For  $h = h_{\min} \dots h_{\max}$  {

Interpolate  $d_{m+h, m-h}(t) \rightarrow d_{m+h, m-h}(t')$  (9).

}

For  $h_1 = h_{\min} \dots h_{\max}$  {

For  $h_2 = (h_1 + 1) \dots h_{\max}$  {

Cross-correlate  $d_{m+h_1, m-h_1}(t')$  and  $d_{m+h_2, m-h_2}(t')$  at lags  $-\Delta_{\max} \dots \Delta_{\max}$ , yielding shift estimate  $\Delta_{h_1 h_2}$ .

If peak correlation  $> x_{\text{thresh}}$  {

$$\mathbf{A} = \begin{bmatrix} \dots & 0 & \overset{(m-h_2)}{-1} & 0 & \dots & 0 & \overset{(m-h_1)}{1} & 0 & \dots & 0 & \overset{(m+h_1)}{1} & 0 & \dots & 0 & \overset{(m+h_2)}{-1} & 0 & \dots \end{bmatrix}$$

$$\mathbf{b} = \begin{bmatrix} \mathbf{b} \\ \Delta_{h_1 h_2} \end{bmatrix}$$

}

}

}

}

Compute the singular-value decomposition  $\mathbf{A} = \mathbf{U}\mathbf{S}\mathbf{V}^T$ ;  $\mathbf{S} = \text{diag}(s_k)$  (the singular values)

Construct  $\mathbf{S}^\dagger = \text{diag}(1/s_k)$  for the  $N - 2$  nonzero  $s_k$ , 0 else

$\tau = \mathbf{V}\mathbf{S}^\dagger\mathbf{U}^T\mathbf{b}$

---

present, the spectrum of the received signals falls cleanly within the bounds dictated by the recording geometry. A smooth, long-correlation-length aberration profile (#1) broadens the spectrum only slightly. Profile #2, with similar amplitude but a shorter correlation length, smears more energy outside the boundary, but more than half of the signal is still inside. Under profile #3, with its rapid, low-amplitude fluctuations, most of the signal remains within the original band while the remainder is spread widely across the rest of the spatial frequencies.

### III. OVERDETERMINED, FAN-FILTERING (OFF) ALGORITHM

For data from an  $N$ -element array, Table I presents the variable definitions and steps needed to derive the aberration profile for a region of interest centered at  $(x_{\text{ROI}}, z_{\text{ROI}})$ . Different 2-D fan filters are applied to each signal set  $d_g(t; s)$ . The angular acceptance range is centered for the zero-offset signal  $d_{s,s}(t)$  from the region of interest, and  $\Delta\rho$  is chosen at least large enough to pass signals at  $h_{\max}$ . Following this, at each midpoint, the common-midpoint signals are corrected for geometric path-length differences according to (9). Within the corrected common-midpoint signals, all pairwise cross-correlations are performed. Time-shift estimates from those pairs having cross-correlation coefficients above some threshold  $x_{\text{thresh}}$  are incorporated into the overdetermined linear system  $\mathbf{A}\tau = \mathbf{b}$ . After every common-midpoint gather has been processed, the  $\mathbf{A}$  matrix is regularized using the singular-value decomposition, and

the least-squares solution for the aberration profile  $\tau$  is obtained [36].

In order to accommodate the greatest possible time shift between a pair of common-midpoint signals, the maximum cross-correlation lag,  $\Delta_{\max}$ , must be at least twice the expected peak-to-peak amplitude of  $\tau$ . (This is because the overall time shift involves four individual-element time shifts.) To prevent bad time-shift estimates due to ‘‘cycle skipping,’’ however,  $\Delta_{\max}$  should be kept as small as possible. Fortunately, a small number of bad estimates in this highly overdetermined system will not perturb the least-squares solution very much.

For cases where  $\Delta_{\max}$  must be set high enough that cycle-skipping in the time-shift estimates becomes problematic, the following correction procedure has been used: First, calculate the error vector  $\mathbf{e}$  and sort it by magnitude. Starting with the largest element of  $\mathbf{e}$ , add or subtract  $1/f_c$  from the corresponding element of  $\mathbf{b}$  for negative or positive error, respectively. Continue for elements of  $\mathbf{e}$  larger than  $\beta$  times the mean error, then stop, calculate an updated error vector, and start the process over. Repeat until the mean error stops decreasing.

For the results presented in the next section,  $\Delta\rho$  was 10 degrees and  $x_{\text{thresh}}$  was 0.5. The offset range  $h_{\min}$  to  $h_{\max}$  was 1 to 12 elements. (Zero-offset data were excluded for simplicity because our data-acquisition procedure routes the  $N$  zero-offset, pulse-echo signals through different analog hardware than the other  $N^2 - N$  signals.) For the  $\mathbf{b}$ -adjustment procedure in the preceding paragraph,  $\beta$  was 3.

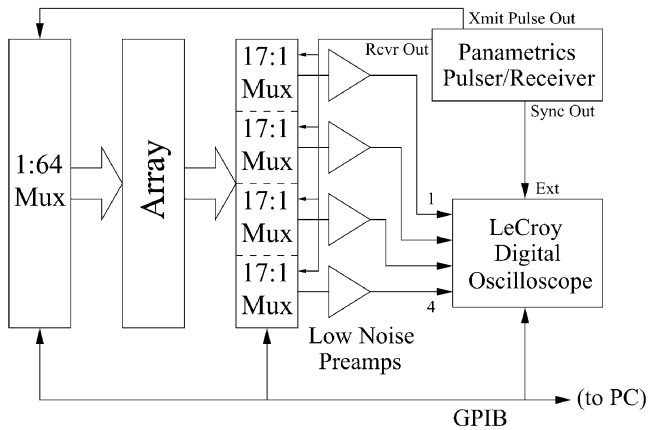


Fig. 7. Apparatus for collecting complete data sets from a 64-element array transducer.

## IV. EXPERIMENTAL PROCEDURES

### A. Acquisition of Complete Data Sets

Most of the complete data sets used in this research were acquired in the Bioacoustics Research Laboratory at the University of Illinois using a 64-element phased-array transducer (2.6-MHz center frequency, 315- $\mu\text{m}$  pitch) and a custom data-acquisition system (Fig. 7). radio frequency (RF) multiplexers (Matrix Systems, Calabasas, CA) permitted the independent selection of single elements on receive or transmit. Transmit pulses were provided by a Panametrics 5800 pulser/receiver (GE Panametrics, Waltham, MA). A GPIB-connected digital oscilloscope (LeCroy, Chestnut Ridge, NY) carried out the tasks of digitization and averaging. Scans were conducted in a tank of degassed water at room temperature.

Individual array elements were selected for receive or transmit by a GPIB-controlled RF multiplexer system. A software application commanded the multiplexers through all 4096 transmit/receive element combinations, acquired waveforms from the digital oscilloscope with 12-bit resolution, and saved the data as a  $64 \times 64 \times N_t$  cube for later processing in MATLAB. signal-to-noise ratio (SNR) was improved by averaging each signal over many transmit pulses, FIR bandpass filtering each signal from 250 kHz to 5 MHz, and 2-D FIR fan filtering (Section II) each of the 64 received wavefields with an angular passband of  $0 \pm 40^\circ$ . The latter operation strongly attenuates undesirable events in the data. These events are either slow waves (such as surface waves) or strong reflections from far-off-axis objects—typically the hardware used to hold the target in position.

### B. Targets for Imaging

A tissue-mimicking phantom (Model #539, ATS Laboratories, Bridgeport, CT) served as the target for most of the data sets. The phantom is a physical model approximating the scattering and attenuation properties of biological tissue. It uses wires and cylindrical structures to simulate point targets and cysts of various sizes placed within speckle-producing background scatter. Anechoic (scatter-free) cysts with diameters of 8, 6, 4, 3, and 2 mm are arranged in five columns. Another

column of cysts are 15 mm in diameter, with scattering gradations from 15 dB above to 15 dB below the background level. The background has a 1450-m/s speed of sound.

The  $\pm 40^\circ$  field of view used here covers the part of the phantom containing cysts with a speckle background. There is only one point target, far to one side, in most of the images. The relative lack of strong, coherent scatterers is intended to make aberration correction more challenging; for some algorithms, these could serve as clear “beacon signals” [13].

### C. Silicone Aberrators

Artificial aberrating structures (Fig. 8) were constructed from GE RTV615, a two-part, room-temperature-vulcanizing silicone rubber. This material has an 1100-m/s speed of sound and an acoustic impedance of approximately 1.1 MRayl [37], thus providing strong refraction without much reverberation. The aberrators have a rippled surface on the underside, created by pouring the liquid silicone into a rippled mold. The mold material was Ivory<sup>TM</sup> soap, carved using pieces of sheet metal that had template curves cut into their edges with a rotary tool.

During scans in the water tank, the aberrators’ ripples were carefully aligned with the array elements. By thus restricting the aberration to one dimension, a fair test of aberration correction was made possible with the 1-D array. (It is well-established that phase aberrations in real tissue can have characteristic correlation lengths in the elevation direction which are much shorter than the typical 1-D array element size [4]. To properly correct for these aberrations, 1.5-D or 2-D arrays are needed [38], [39], along with 2-D versions of the aberration-correction algorithms. While computationally daunting, these extensions are reasonably straightforward.)

The complete data sets used for the results in Section V are listed in Table II in approximate order of aberration-correction difficulty. All of the data sets were collected in-house except for the Michigan data, which comes from the Biomedical Ultrasound Laboratory (BUL) at the University of Michigan [40]. This data set is the “2X” aberrator example from the original work on the NNCC algorithm [14]. It was used here to verify the implementation of NNCC and to provide a comparison with the locally collected silicone aberrator data sets. Because this data set was collected without averaging, it also allowed the evaluation of algorithms at low SNR. The RTV aberrators in [14] were molded onto the transducer surface, so the aberration in the Michigan data conforms closely to the phase-screen model. By contrast, the nonzero stand-off distance from the aberrators in the thin- and thick-aberrator data sets, combined with the significant thickness of the aberrators themselves, means that the aberration in these data sets is more angle-dependent (smaller isoplanatic patch sizes).

### D. Derivation of Aberration Profiles

The processed data were passed to a collection of programs implementing different phase-screen aberration-correction algorithms. Each algorithm was given a list of target regions of interest (ROIs) for which to perform aberration correction. Given a complete data set as input, it then provided a set of aberration corrections as output. Each correction contained the length- $N$  aberration profile  $\tau$  and the parameters estimated from the least-squares, best-fit hyperbola (see Section I). These auxiliary para-

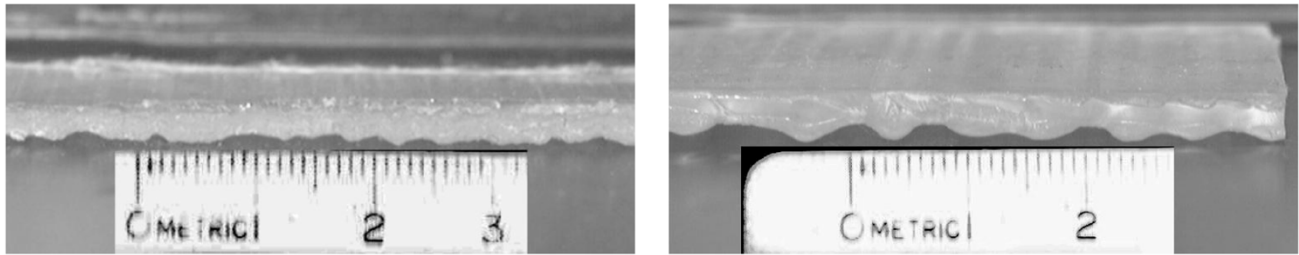


Fig. 8. Profile views of the “thin” and “thick” aberrators.

TABLE II  
COMPLETE DATA SETS USED FOR THE ABERRATION-CORRECTION EXPERIMENTS

Name	Source	$f_c$ (MHz)	Averaging	Aberrator	Thickness (mm, max)	Ripple (mm, p-p)	Correlation length (mm)	Stand-off dist. (mm)	$\tau_{p-p}$ (ns)
No aberration	BRL <sup>1</sup>	2.6	200x	none	—	—	—	—	—
Michigan data	BUL <sup>2</sup>	3.3	none	grooved RTV	1.5	0.8	1.2	~ 0?	280
Thin aberrator	BRL <sup>1</sup>	2.6	160x	“thin” RTV	3	1	2.4	6	180
Thick aberrator	BRL <sup>1</sup>	2.6	200x	“thick” RTV	4	2	2.9	9	~ 300

<sup>1</sup>Bioacoustics Research Lab, University of Illinois

<sup>2</sup>Biomedical Ultrasound Laboratory, University of Michigan

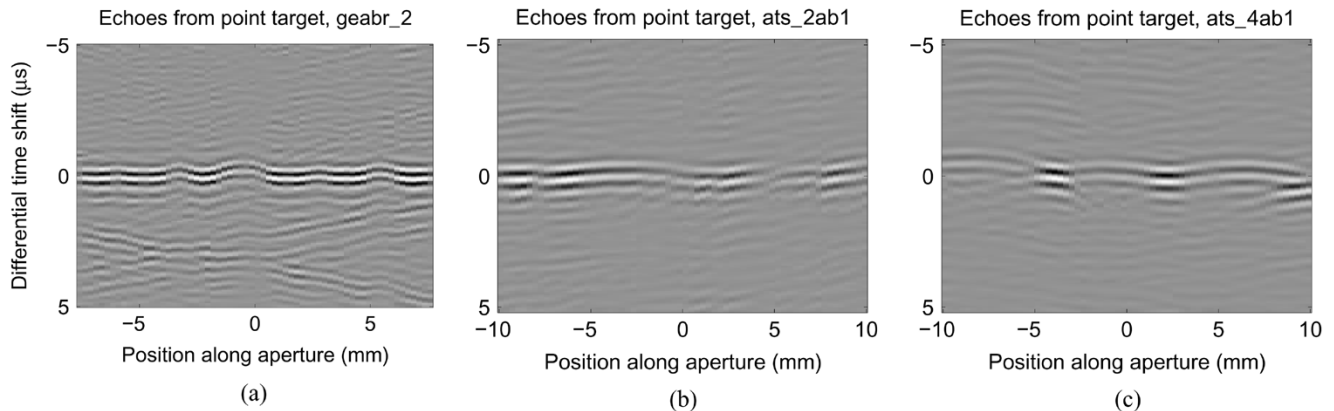


Fig. 9. Plots of the echo wavefield received from point targets in the three aberrated data sets show increasing diffraction and amplitude fluctuation effects from (a) to (c), hampering aberration correction. (From left to right: Michigan data, thin aberrator, thick aberrator. Linear amplitude scale.)

meters were used to automatically exclude some of the profiles from further processing; specifically, profiles were discarded when the estimated speed of sound had an imaginary component, or when the peak value of a profile exceeded some threshold (arbitrary, but constant for a given data set). Typically, these conditions indicated a failure for the aberration-correction algorithm to converge.

The OFF algorithm was described in detail in Section III. Three previously published algorithms, representative of three approaches to phase-aberration correction, were also compared on the same data: The NNCC algorithm [13], [14] (iterative, full-aperture transmit focus), the speckle brightness algorithm [16]–[18] (image quality metric), and the NFSR algorithm with subarrays [22], [23] (common-midpoint signals). Implementation details are provided in [33].

### E. Imaging

Images were formed from the complete data sets and the derived aberration profiles using delay-and-sum beamforming at each point on transmit and receive, i.e., dynamic focus on transmit and receive. Hamming apodization was used on the

transmit aperture. Each range line of the beamformed images was envelope-detected by applying the Hilbert transform and taking the magnitude of the analytic signal. Finally, an approximate gain correction was applied by multiplying each pixel by  $(r/r_{\min})^2$ , the squared ratio of the current range to the minimum range in the image.

The imaging process was decoupled from aberration correction. If an image at a constant speed of sound was desired, the ideal hyperbolic operators were used. Otherwise, the various aberration-correction codes supplied a collection of estimated profiles, and the locations for which they were derived, to the imaging code. For each point in the image, the algorithm selected two aberration profiles valid at the point’s depth and located on either side of it in azimuth angle. If the profiles differed primarily by a lateral shift, as evidenced by a high cross-correlation value at some small lag, an interpolated profile was derived: The average of the lined-up profiles was used, shifted by a linearly interpolated distance based on the azimuth angles of the two aberration profile locations and the image point between them. In cases where the two aberration profiles did not appear correlated, or the image point lay outside the region populated by profiles, the profile nearest the point’s location was used.

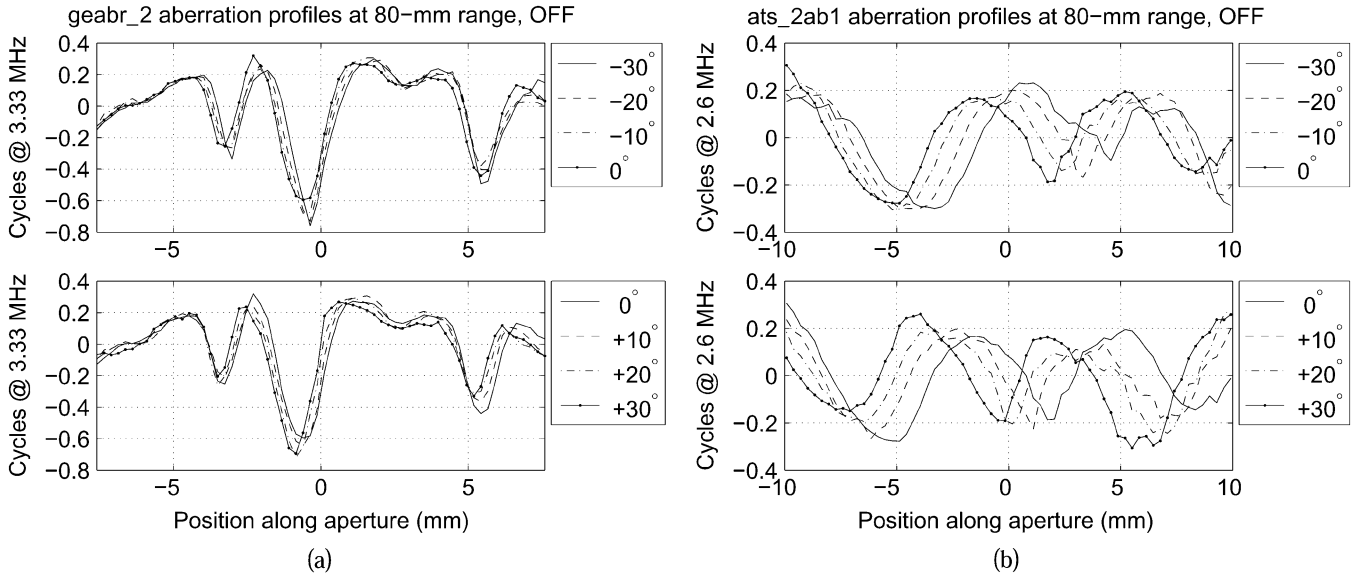


Fig. 10. (a) The OFF-estimated aberration profiles for the Michigan data are almost angle-independent, indicating very-near-field aberration. (b) By contrast, the aberration profiles from the thin aberrator vary considerably with azimuth steering; accurate estimates at many azimuth angles are, thus, needed for good imaging performance.

This occasionally led to obvious discontinuities in the finished images, especially far off-axis, when the quality of the aberration profiles was poor or the profiles gave insufficient coverage.

The method of image presentation was carefully chosen to ensure fairness. All of the images were drawn over a 50-dB dynamic range. The 0-dB point is constant within each set of six comparison images, and was chosen to place the background speckle in the upper quarter of the brightness range. This saturated the point reflectors but provided the best contrast between the scatter-free regions and background speckle.

## V. RESULTS

### A. Michigan Data

The wavefields in Fig. 9 show the fluctuations in arrival time and amplitude of the received echoes after the application of nominal focusing delays. The aberration in the Michigan data caused minor amplitude fluctuations along the aperture [Fig. 9(a)]; otherwise, it conforms closely to the expectations of the phase-screen model. A look at the OFF-derived aberration profiles for a wide range of steering angles [Fig. 10(a)] confirms that the aberration was in the extreme near-field; there was very little change in the profile with  $\theta$ . This was expected, given the description in [14] of a thin silicone aberrator attached directly to the surface of the array transducer. (The claim that these profiles are accurate is supported by the fact that the OFF-derived profiles were able to correct a wide range of azimuths in the image; also, a strong  $\theta$ -dependence was observed for the other data sets.)

The original, aberrated, and four corrected images using aberration profiles from the NNCC, speckle brightness, NFSR subarray, and OFF algorithms are shown in Fig. 11. Forty-five ROIs were selected for  $\theta = -40^\circ, -30^\circ, \dots, 40^\circ$ , and  $r = 40, 60, \dots, 120$  mm. There were 27 profiles used for the speckle brightness and OFF images, 18 for the NFSR image, and 14 for the NNCC image.

The best images were provided by the speckle-brightness and OFF algorithms. All of the algorithms apparently had trouble finding correct operators for the far-right edge of the image, perhaps because of the bright point targets nearby. The NNCC image

matches the published image in [14] except for the anechoic cyst at 70-mm depth. With *a priori* information that the aberration profiles are mostly independent of  $\theta$ , the  $\theta = 0^\circ$  profiles could have been used at all angles, instead of attempting to correct for different angles. In this case the image would improve.

Because the Michigan data was acquired without any averaging [40], it offered a good opportunity to compare the low-SNR performance of the various algorithms in a setting similar to that which might be encountered in clinical practice. It is often believed that aberration correction using complete data sets is infeasible due to the noise penalty incurred by transmitting and receiving on single elements. As seen in Fig. 12, this is not necessarily the case. The performance of both algorithms did indeed suffer at large depths, but OFF did better than NNCC. An authoritative comparison would require NNCC to be implemented online with a true transmit focus, rather than the synthetic aperture used here, because doing so would give it an additional SNR advantage which is not available to OFF. Still, this experiment suggests that the redundancy in complete data sets may be exploited to compensate for lower SNR.

Contrast-to-noise ratios (CNRs) (see Table III) were calculated for the central cyst at 90-mm depth using the three image regions labeled in the “original” image of Fig. 11

$$\text{CNR}_{a/b} = 20 \log_{10} \left( \frac{\sum_a \text{Image}}{\sum_b \text{Image}} \right). \quad (24)$$

(The NFSR subarray algorithm is not included in Table III because it shifted the central cyst relative to the CNR calculation regions, making a fair comparison difficult.) A difference of 2 dB is seen when comparing the CNR measured with background regions to the right and the left of the cyst; however, the relative changes are consistent. The differences between the NNCC, speckle brightness, and OFF algorithms are relatively minor compared to the significant gap between the best corrected image and the original, unaberrated image. This may be due to the amplitude fluctuations or waveform distortions imposed by the aberrator, which were not addressed by any of the

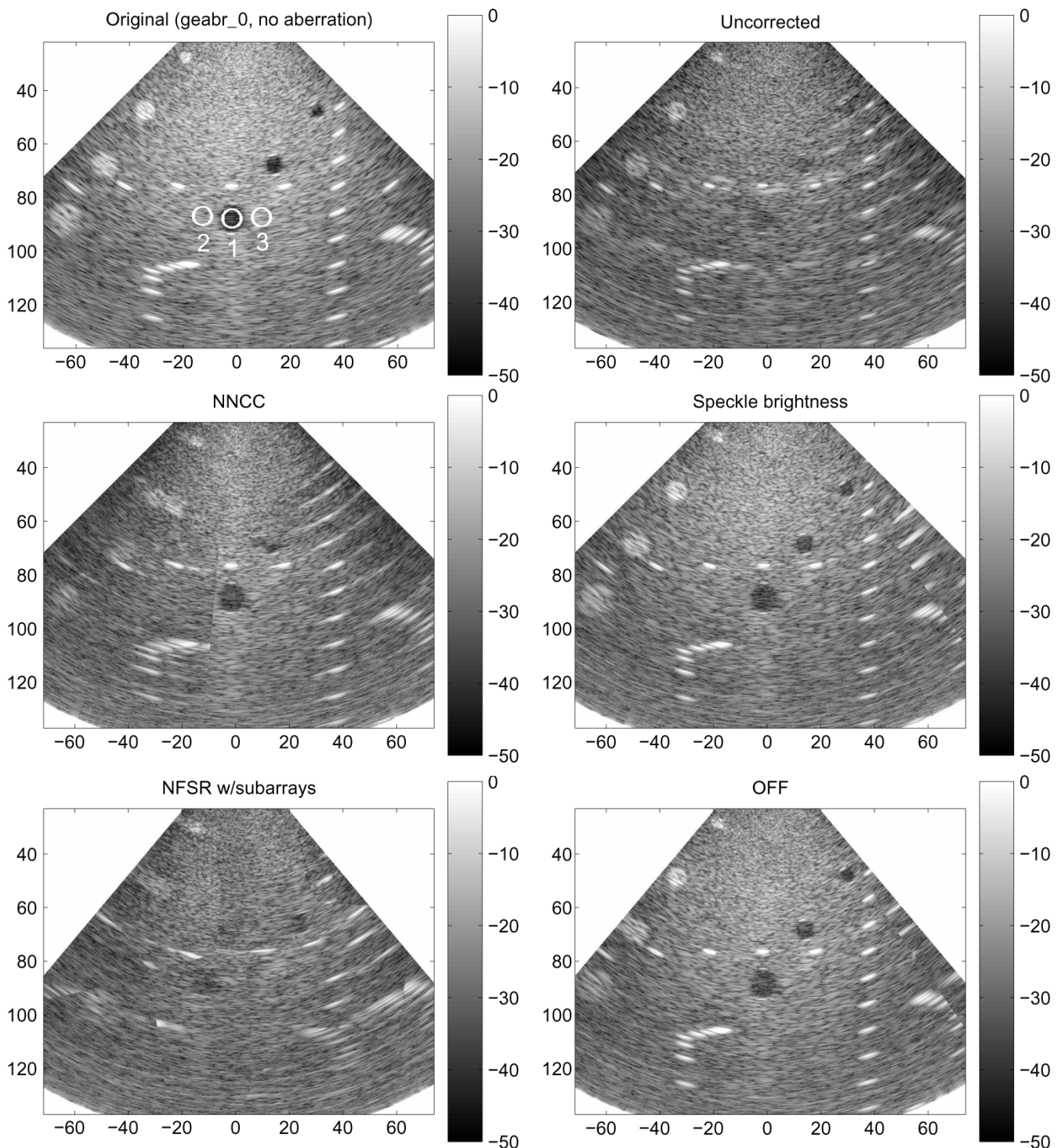


Fig. 11. Images of the Michigan data—original, uncorrected, and corrected with aberration profiles supplied by four different algorithms (50-dB log scale; axis labels in millimeters). Superimposed on the image of the original data set are the numbered regions for CNR measurements (Table III).

correction schemes. Note that CNR values were not calculated for the next two data sets, because the cysts are too small, relative to the imaging resolution, to allow a statistically significant comparison.

### B. Thin Aberrator

A sample received wavefield [Fig. 9(b)] for this data set exhibits amplitude fluctuations similar to those in the Michigan

data. More striking are the near-discontinuities caused by diffraction, especially toward the right-hand side of the aperture. These may cause difficulty for algorithms like NNCC which only consider adjacent element signals.

The aberrator in this case was not located at the array surface, but about 6 mm away from it. Consequently, the aberration profiles were strongly  $\theta$ -dependent [Fig. 10(b)]. Notice that the profiles are almost completely out of phase between the left and right steering extremes. Profiles over the full range of angles

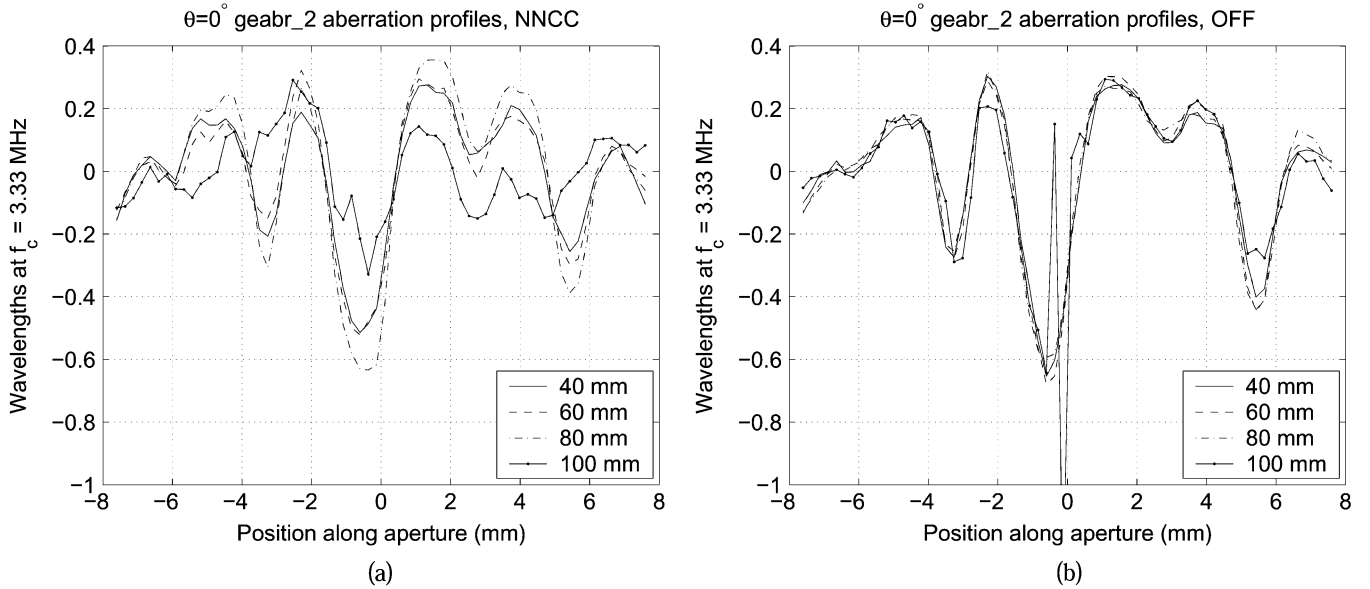


Fig. 12. Comparing the estimated aberration profiles at several depths using NNCC (a) and OFF (b) shows that OFF performed better than NNCC at large depths, even broadside to the array. Note that the Michigan data were collected using no averaging, so the available SNR should be similar to a clinical situation.

are clearly necessary to achieve good correction throughout the image.

The original, aberrated, and four corrected images from the different algorithms are shown in Fig. 13. Twenty-eight ROIs were specified for  $\theta = -30^\circ, -20^\circ, \dots, 30^\circ$ , and  $r = 40, 60, \dots, 100$  mm. There were 28 profiles used for the speckle brightness and OFF images, 24 for the NNCC image, and 13 for the NFSR image.

For this data set, OFF yielded the best image. (Examine the visibility of the deeper cysts, the definition of the shallower cysts, and the correction of the large extra-scattering cysts on the right-hand side.) The speckle brightness algorithm performed well also. NFSR and NNCC were both hampered by an inability to find the correct aberration profiles at large angles from the array normal.

### C. Thick Aberrator

This data set was obtained by scanning the ATS phantom through the thicker silicone aberrator at 9-mm stand-off distance from the transducer. Notice the strong amplitude fluctuations and obvious diffraction artifacts in the received wavefield from a point reflector [Fig. 9(c)]. This was by far the most difficult aberration to correct. Because none of the phase-aberration correction algorithms had excellent performance on this data set, the true aberration profiles are not known, but an examination of the various estimates suggests that the peak-to-peak aberration,  $\tau_{p-p}$ , was about 300 ns (Table II), not dramatically larger than the 180 ns for the thin aberrator data. The difference may have been due to the increased distance (9 mm) from the transducer.

The original, aberrated, and four corrected images from the different algorithms are shown in Fig. 14. Twenty-eight ROIs were specified for  $\theta = -30^\circ, -20^\circ, \dots, 30^\circ$ , and  $r = 40, 60, \dots, 100$  mm. There were 28 profiles used for the speckle brightness image, 25 for the NNCC image, 23 for the NFSR image, and 21 for the OFF image.

TABLE III  
CNR MEASUREMENTS FOR LABELED REGIONS 2 AND 3 RELATIVE TO REGION 1 IN MICHIGAN DATA

Algorithm or data set	CNR <sub>2/1</sub> (dB)	CNR <sub>3/1</sub> (dB)
Original	17.8	19.9
Uncorrected	4.2	6.2
NNCC	10.3	12.2
Speckle brightness	11.8	13.2
OFF	11.8	14.0

Although the speckle brightness and NNCC algorithms yielded marginal image improvement, only the OFF algorithm was successful in revealing numerous anechoic cysts. The cause of the bright arcs in the upper right-hand corner of the images is unknown.

## VI. DISCUSSION

The proposed algorithm is very similar to the approach described by Taner *et al.* for the seismic statics problem [27], the key addition being the angle-selectivity afforded by fan filtering. Like the linear system described in that work, the  $\mathbf{A}$  matrix in OFF turns out to be rank-deficient. In this formulation, the rank is always  $N - 2$ , implying that the solution for  $\tau$  is indeterminate by a linear component. Although surprising at first, this fact has an intuitive explanation.

First, note that because the system is built up from pair-wise relative shift estimates between signals, the solution for  $\{\tau_k, k = 1, \dots, N\}$  is clearly insensitive to an overall constant shift. Thus,  $\{\tau_k + C, k = 1, \dots, N\}$  is also a solution for any constant  $C$ , because this does not change the relative time shifts between signals. Now consider any single row in  $\mathbf{A}$ . Because the pair of signals has the same midpoint, the contribution of any linear component in  $\tau$  is canceled out by the symmetry of the equation—the displacement of transmitters is equal and opposite to the displacement of receivers. (If we were not restricted to common-midpoint signals, this would not be true, and  $\mathbf{A}$  would have rank  $N - 1$ .)

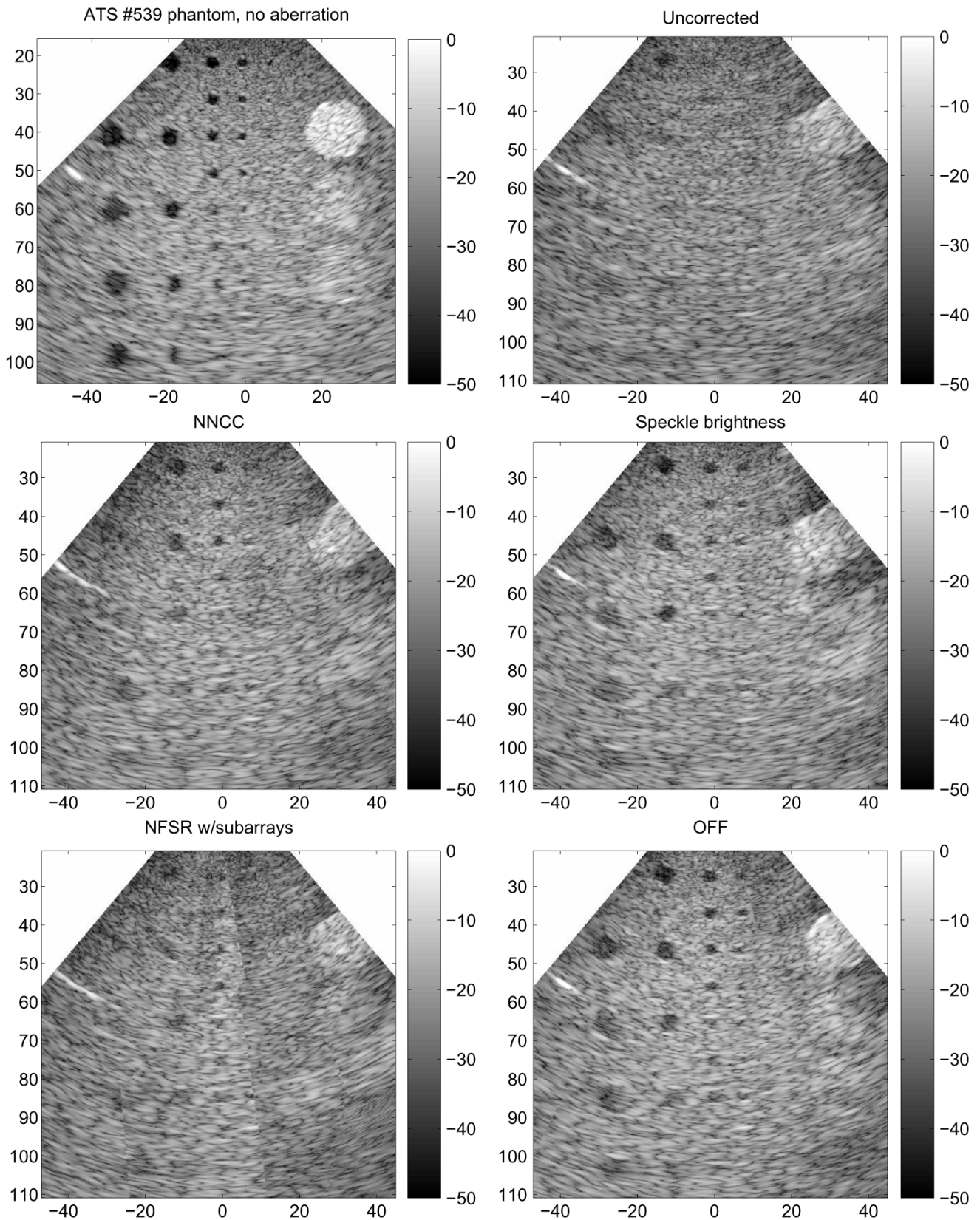


Fig. 13. Images of the thin aberrator data—original (no aberration), uncorrected, and corrected with aberration profiles supplied by four different algorithms (50-dB log scale; axis labels in millimeters).

The rank-deficiency of  $\mathbf{A}$  does not seem to be problem in practice. All of the robustness benefits from a highly over-determined system still apply. Using the singular-value decom-

position yields the minimum-norm solution, which will be the true aberration profile with any linear component subtracted out. To first order, a linear tilt of the focusing delays is equivalent

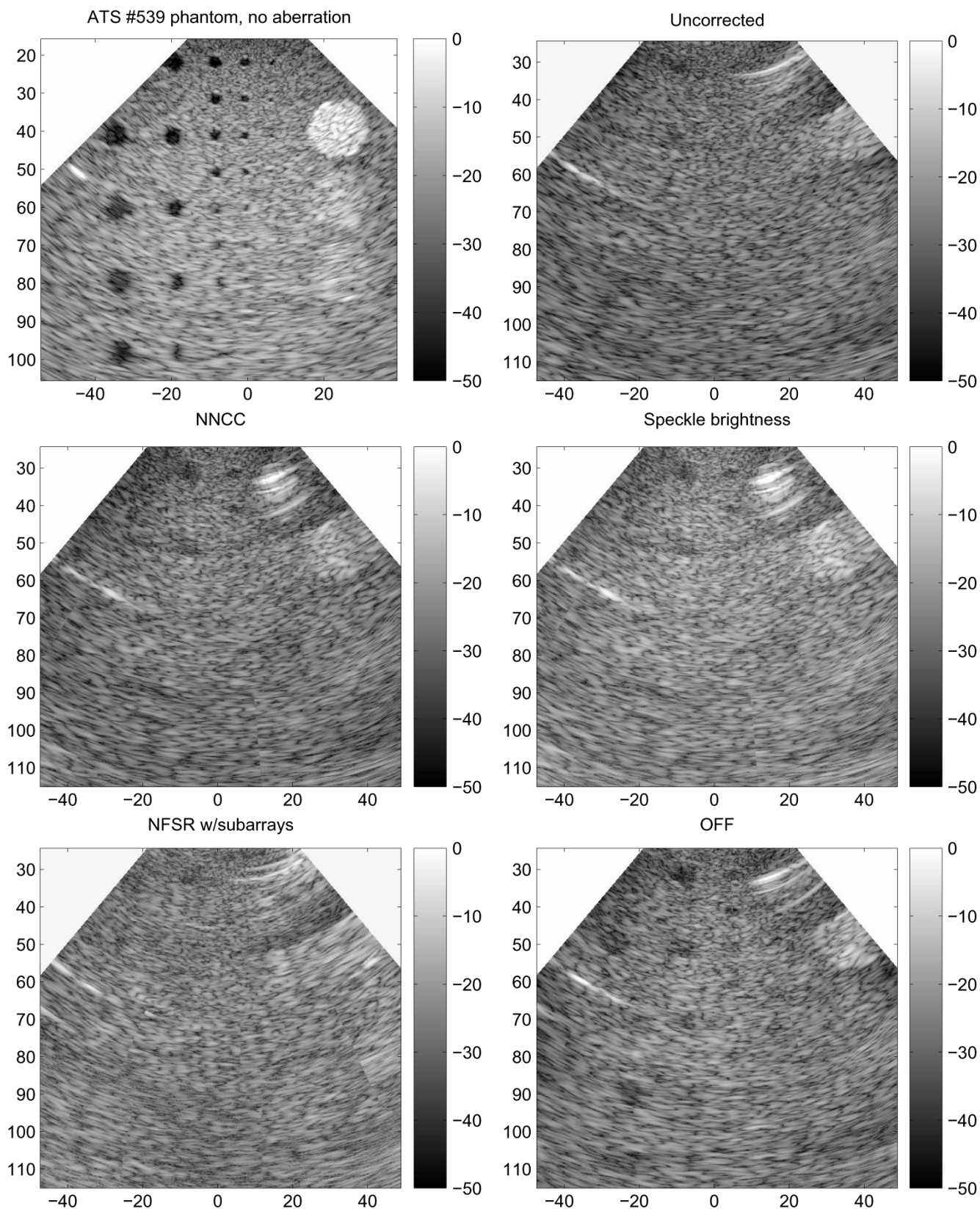


Fig. 14. Images of the thick aberrator data—original (no aberration), uncorrected, and corrected with aberration profiles supplied by four different algorithms (50-dB log scale; axis labels in millimeters).

to a steering-angle change, and the addition of a constant is equivalent to a change in depth. Because these terms are always small (on the same order as the aberrating delays), the quality

of focusing in that neighborhood will not be affected. It is possible, however, that mismatches could be observed when trying to composite an image from many isoplanatic patches.

As noted in the previous section, the least-squares solution is robust to a small number of bad time-shift estimates. Despite this, experiments suggest that this algorithm's performance is ultimately limited by "cycle skipping"—one-period errors in the time-shift estimates. As aberration becomes more severe, the maximum cross-correlation lag ( $\Delta_{\max}$ ) must be increased, and one-period errors become more likely. If the solution scheme could be modified to exploit the fact that most of the time-shift estimates are still correct modulo one period, the overall performance might be significantly improved. The post-processing, **b**-adjustment step is an improvement, but not an optimal solution. A different strategy would be to view this as a non-linear optimization problem. In the context of the seismic statics problem, a form of simulated annealing has been shown to reach good solutions when cycle skipping would otherwise be troublesome [41].

The experimental results indicate that the greatest error in the derived aberration profiles occurs near the ends of the aperture. This is to be expected, because there are fewer offsets and hence fewer equations available to constrain the profile there. It may be beneficial, then, to employ a larger aperture for aberration correction, then throw away a handful of elements at each end and image using the central part of the aperture where the aberration profile is more accurate.

The effect of iteration on OFF remains to be investigated. In cases of severe aberration, a partially correct estimated profile from the first iteration could be applied to the raw data prior to the second iteration. Correcting some or most of the aberration prior to fan filtering would reduce the spreading effect of aberration in spatial frequency, possibly leading to a better aberration estimate.

## VII. CONCLUSION

Tissue-induced aberration is still a problem plaguing medical ultrasound imaging. Although solutions based on single-valued focusing operators cannot perfectly restore diffraction-limited resolution, our results demonstrate that significant improvement over previous results is possible.

Concepts borrowed from other imaging disciplines can provide new insights into the aberration problem in medical ultrasound; in particular, some of the same issues have been studied for many years to improve acoustic imaging of the inhomogeneous Earth. Invariably, such insights also improve the understanding of existing approaches in the medical ultrasound literature.

The tremendous redundancy of a complete data set can be exploited for phase-aberration correction by analyzing the time shifts on common-midpoint gathers. Although the wide-angle, random-scattering nature of medical ultrasound targets has limited the accuracy and robustness of this approach in the past, prefiltering the data with 2-D fan filters can mitigate these problems. The resulting algorithm (OFF) was able to outperform at least some of the existing phase-aberration correction algorithms in experiments with rubber aberrators and phantom targets.

This work has several implications for future aberration-correction research. First, imaging with single-valued focusing operators may be able to correct for most of the aberration encountered in soft tissues. Our results demonstrate obvious im-

provement under the phase-screen model, and there is reason to believe that further improvement is possible without moving to a more complicated model. Second, increasing aperture should not be viewed merely as a source of aberration, but as an opportunity to do a better job of correcting it. Even if a reduced aperture is used for imaging, the extra aperture can provide more information for aberration correction. Third, the noise penalty for using complete data sets may not be as serious a problem as conventionally assumed. The extra information contained in the signals partially compensates for this problem. Finally, the performance of hybrid algorithms should be investigated, where phase-aberration estimates from common-midpoint signals in a complete data set are used to obtain a good initial transmit focus, followed by iterative transmit focusing updates.

If aberration correction based on complete data is to move beyond phantom-based experiments, the data must be acquired much more rapidly than they were in the present experiments. Future research should investigate real-time collection of complete data, possibly using coded excitation to increase the SNR. If this is successful, data collected in clinical settings could be used to validate the aberration-correction algorithm on biological targets.

The complete data sets and MATLAB code used for this research are freely available at the Bioacoustics Research Lab web site [42].

## ACKNOWLEDGMENT

The authors would like to acknowledge the support of many people in the Bioacoustics Research Lab that has made this research project a success; in particular, they thank J. Blue, D. Matthews, R. Miller, and M. Johnson for their assistance with the experimental work. Many helpful suggestions and critiques were given by Joseph Dellinger and his colleagues in BP's Upstream Technology Group, by Y. Li, A. Paplinski, and the reviewers.

## REFERENCES

- [1] S. A. Goss, R. L. Johnston, and F. Dunn, "Comprehensive compilation of empirical ultrasonic properties of mammalian tissues," *J. Acoust. Soc. Amer.*, vol. 64, no. 2, pp. 423–457, Aug. 1978.
- [2] —, "Comprehensive compilation of empirical ultrasonic properties of mammalian tissues, II," *J. Acoust. Soc. Amer.*, vol. 68, no. 1, pp. 93–108, July 1980.
- [3] Y. Sumino and R. C. Waag, "Measurements of ultrasonic pulse arrival time differences produced by abdominal wall specimens," *J. Acoust. Soc. Amer.*, vol. 90, no. 6, pp. 2924–2930, Dec. 1991.
- [4] L. M. Hinkelman, D.-L. Liu, L. A. Metlay, and R. C. Waag, "Measurements of ultrasonic pulse arrival time and energy level variations produced by propagation through abdominal wall," *J. Acoust. Soc. Amer.*, vol. 95, no. 1, pp. 530–541, Jan. 1994.
- [5] M. Moshfeghi and R. C. Waag, "In vivo and in vitro ultrasound beam distortion measurements of a large aperture and a conventional aperture focussed transducer," *Ultrasound Med. Biol.*, vol. 14, no. 5, pp. 415–428, 1988.
- [6] Q. Zhu and B. D. Steinberg, "Large-transducer measurements of wavefront distortion in the female breast," *Ultrason. Imag.*, vol. 14, pp. 276–299, 1992.
- [7] C. Dorme and M. Fink, "Focusing in transmit-receive mode through inhomogeneous media: The time reversal matched filter approach," *J. Acoust. Soc. Amer.*, vol. 98, no. 2, pp. 1155–1162, Aug. 1995.
- [8] —, "Ultrasonic beam steering through inhomogeneous layers with a time reversal mirror," *IEEE Trans. Ultrason., Ferroelect., Freq. Contr.*, vol. 43, pp. 167–175, Jan. 1996.

- [9] M. Tanter, J.-F. Aubry, J. Gerber, J.-L. Thomas, and M. Fink, "Optimal focusing by spatio-temporal inverse filter: Basic principles," *J. Acoust. Soc. Amer.*, vol. 110, no. 1, pp. 37–47, July 2001.
- [10] J.-F. Aubry, M. Tanter, J. Gerber, J.-L. Thomas, and M. Fink, "Optimal focusing by spatio-temporal inverse filter: Experiments—Application to focusing through absorbing and reverberating media," *J. Acoust. Soc. Amer.*, vol. 110, no. 1, pp. 48–58, July 2001.
- [11] D. H. Huang and J. Tsao, "Analysis and correction of ultrasonic wavefront distortion based on a multilayer phase-screen model," *IEEE Trans. Ultrason., Ferroelect., Freq. Contr.*, vol. 49, pp. 1686–1703, Dec. 2002.
- [12] F. Lin and R. C. Waag, "Estimation and compensation of ultrasonic wavefront distortion using a blind system identification method," *IEEE Trans. Ultrason., Ferroelect., Freq. Contr.*, vol. 49, pp. 739–755, June 2002.
- [13] S. W. Flax and M. O'Donnell, "Phase-aberration correction using signals from point reflectors and diffuse scatterers: Basic principles," *IEEE Trans. Ultrason., Ferroelect., Freq. Contr.*, vol. 35, pp. 758–767, Nov. 1988.
- [14] M. O'Donnell and S. W. Flax, "Phase-aberration correction using signals from point reflectors and diffuse scatterers: Measurements," *IEEE Trans. Ultrason., Ferroelect., Freq. Contr.*, vol. 35, pp. 768–774, Nov. 1988.
- [15] G. C. Ng, P. D. Freiburger, W. F. Walker, and G. E. Trahey, "A speckle target adaptive imaging technique in the presence of distributed aberrations," *IEEE Trans. Ultrason., Ferroelect., Freq. Contr.*, vol. 44, pp. 140–151, Jan. 1997.
- [16] L. Nock, G. E. Trahey, and S. W. Smith, "Phase aberration correction in medical ultrasound using speckle brightness as a quality factor," *J. Acoust. Soc. Amer.*, vol. 85, no. 5, pp. 1819–1833, May 1989.
- [17] G. Trahey, D. Zhao, J. A. Miglin, and S. W. Smith, "Experimental results with a real-time adaptive ultrasonic imaging system for viewing through distorting media," *IEEE Trans. Ultrason., Ferroelect., Freq. Contr.*, vol. 37, pp. 418–427, Sept. 1990.
- [18] D. Zhao and G. E. Trahey, "Comparisons of image quality factors for phase aberration correction with diffuse and point targets: Theory and experiments," *IEEE Trans. Ultrason., Ferroelect., Freq. Contr.*, vol. 38, no. 2, pp. 125–132, Mar. 1991.
- [19] D. Rachlin, "Direct estimation of aberrating delays in pulse-echo imaging systems," *J. Acoust. Soc. Amer.*, vol. 88, no. 1, pp. 191–198, July 1990.
- [20] Y. Li, "Phase aberration correction using near-field signal redundancy—Part I: Principles," *IEEE Trans. Ultrason., Ferroelect., Freq. Contr.*, vol. 44, pp. 355–371, Mar. 1997.
- [21] Y. Li, D. Robinson, and D. Carpenter, "Phase aberration correction using near-field signal redundancy—Part II: Experimental results," *IEEE Trans. Ultrason., Ferroelect., Freq. Contr.*, vol. 44, pp. 372–379, Mar. 1997.
- [22] Y. Li, "Small element array algorithm for correcting phase aberration using near-field signal redundancy—Part I: Principles," *IEEE Trans. Ultrason., Ferroelect., Freq. Contr.*, vol. 47, pp. 29–48, Jan. 2000.
- [23] Y. Li and B. Robinson, "Small element array algorithm for correcting phase aberration using near-field signal redundancy—Part II: Experimental results," *IEEE Trans. Ultrason., Ferroelect., Freq. Contr.*, vol. 47, pp. 49–57, Jan. 2000.
- [24] A. J. Berkhout, "Pushing the limits of seismic imaging, part I: Prestack migration in terms of double dynamic focusing," *Geophysics*, vol. 62, no. 3, pp. 937–953, May–June 1997.
- [25] O. Yilmaz, *Seismic Data Analysis*. Tulsa, OK: Soc. Exploration Geophysicists, 2001.
- [26] J. A. Hileman, P. Embree, and J. C. Pflueger, "Automated static corrections," *Geophysical Prospecting*, vol. 16, pp. 326–358, 1968.
- [27] M. T. Taner, F. Koehler, and K. A. Alhilali, "Estimation and correction of near-surface time anomalies," *Geophysics*, vol. 39, no. 4, pp. 441–463, Aug. 1974.
- [28] D.-L. Liu and R. C. Waag, "Correction of ultrasonic wavefront distortion using backpropagation and a reference waveform method for time-shift compensation," *J. Acoust. Soc. Amer.*, vol. 96, no. 2, pp. 649–660, Aug. 1994.
- [29] F. Audebert, D. Nichols, T. Rekdal, B. Biondi, D. Lumley, and H. Urdaneta, "Imaging complex geologic structure with single-arrival Kirchhoff prestack depth migration," *Geophysics*, vol. 62, no. 5, pp. 1533–1543, Sept.–Oct. 1997.
- [30] R. Mallart and M. Fink, "The van Cittert-Zernike theorem in pulse echo measurements," *J. Acoust. Soc. Amer.*, vol. 90, no. 5, pp. 2718–2727, Nov. 1991.
- [31] ———, "Adaptive focusing in scattering media through sound-speed inhomogeneities: The van Cittert-Zernike approach and focusing criterion," *J. Acoust. Soc. Amer.*, vol. 96, no. 6, pp. 3721–3732, Dec. 1994.
- [32] J. F. Claerbout, *Imaging the Earth's Interior*. Palo Alto, CA: Blackwell Scientific, 1985.
- [33] M. A. Haun, "New approaches to aberration correction in medical ultrasound imaging," Ph.D. dissertation, Univ. Illinois at Urbana-Champaign, Urbana, IL, 2003. [Online]. Available: <http://www.brl.uiuc.edu/>
- [34] T. S. Huang, "Two-dimensional windows," *IEEE Trans. Audio Electroacoust.*, vol. AU-20, pp. 88–89, Mar. 1972.
- [35] J. G. Proakis and M. Salehi, *Communication Systems Engineering*. Englewood Cliffs, NJ: Prentice-Hall, 1994.
- [36] W. H. Press, B. P. Flannery, S. A. Teukolsky, and W. T. Vetterling, *Numerical Recipes in C*. New York: Cambridge University Press, 1990.
- [37] Onda Corp., Sunnyvale, CA. (2003) Acoustic Properties of Rubbers. [Online]. Available: <http://www.ondacorp.com/tables/Rubbers.pdf>
- [38] J. C. Laceyfield and R. C. Waag, "Time-shift estimation and focusing through distributed aberration using multirow arrays," *IEEE Trans. Ultrason., Ferroelect., Freq. Contr.*, vol. 48, no. 6, pp. 1606–1624, Nov. 2001.
- [39] D.-L. Liu, "Element size effect on phase aberration correction," *IEEE Trans. Ultrason., Ferroelect., Freq. Contr.*, vol. 49, no. 9, pp. 1212–1221, Sept. 2002.
- [40] Biomed. Ultrason. Lab., Univ. Michigan, Ann Arbor, MI. (2001) Online ultrasound data. [Online]. Available: [http://bul.eecs.umich.edu/ultrasound\\_data.html](http://bul.eecs.umich.edu/ultrasound_data.html)
- [41] D. H. Rothman, "Large near-surface anomalies, seismic reflection data, and simulated annealing," Ph.D. dissertation, Stanford Univ., Stanford, CA, 1985. [Online]. Available: <http://sepwww.stanford.edu/theses/sep45/>
- [42] Bioacoust. Research Lab., Univ. Illinois at Urbana-Champaign, Urbana, IL. (2003) Downloads. [Online]. Available: <http://www.brl.uiuc.edu/>